

KEPLA: A Knowledge-Enhanced Deep Learning Framework for Accurate Protein-Ligand Binding Affinity Prediction

Han Liu¹, Keyan Ding², Peilin Chen¹, Yinwei Wei³, Liqiang Nie⁴, Dapeng Wu¹, and Shiqi Wang^{1,*}

¹Department of Computer Science, City University of Hong Kong, Hong Kong (SAR), China

²ZJU-Hangzhou Global Scientific and Technological Innovation Center, Zhejiang University, Hangzhou, China

³School of Software, Shandong University, Jinan, China

⁴College of Informatics, Harbin Institute of Technology (Shenzhen), Shenzhen, China

*corresponding author: Shiqi Wang

e-mail: hanliu.sdu@gmail.com; dingkeyan@zju.edu.cn; plchen3@cityu.edu.hk; weiyinwei@hotmail.com;

nieliqiang@gmail.com; dapengwu@cityu.edu.hk; shiqiwang@cityu.edu.hk

ABSTRACT

Accurate prediction of protein-ligand binding affinity is critical for drug discovery. While recent deep learning approaches have demonstrated promising results, they often rely solely on structural features of proteins and ligands, overlooking their valuable biochemical knowledge associated with binding affinity. To address this limitation, we propose KEPLA, a novel deep learning framework that explicitly integrates prior knowledge from Gene Ontology and ligand properties to enhance prediction performance. KEPLA takes protein sequences and ligand molecular graphs as input and optimizes two complementary objectives: (1) aligning global representations with knowledge graph relations to capture domain-specific biochemical insights, and (2) leveraging cross attention between local representations to construct fine-grained joint embeddings for prediction. Experiments on two benchmark datasets across both in-domain and cross-domain scenarios demonstrate that KEPLA consistently outperforms state-of-the-art baselines. Furthermore, interpretability analyses based on knowledge graph relations and cross attention maps provide valuable insights into the underlying predictive mechanisms.

Introduction

The prediction of protein-ligand binding affinity (PLA) has been widely considered as one of the most important tasks in computational drug discovery¹. Here, ligands are usually drug candidates, including small molecules and biologics, which can interact with proteins as agonists or inhibitors in biological processes to cure diseases. Given a protein, we want to understand how well a ligand can interact with this protein. The strength of interaction between them can be quantified as a numerical score (called the binding affinity), which potentially determines whether a ligand can effectively influence the protein (for example, to inactivate a protein to cure a disease). Although experimental methods² can measure binding affinity, these biological tests are laborious and time-consuming. Thus, *in silico* predictive approaches have become increasingly necessary and received widespread attention³. With *in silico* approaches, binding affinities can be quickly predicted in the early stage of drug discovery. The predicted binding affinities can help rank drug candidates and prioritize the appropriate ones for more precise subsequent tests to accelerate the drug screening process, instead of applying costly biological methods directly to screen the entire pool of numerous candidate molecules⁴.

Recently, along with their success in other areas, deep learning approaches have rapidly progressed for computational PLA prediction⁵. The scientific community has primarily divided these deep learning approaches into interaction-based and interaction-free methodologies, which are distinguished by whether they rely on physical interactions to inform predictions. Interaction-based approaches make predictions based on the known three-dimensional (3D) structures of complexes and the physical interactions between proteins and ligands⁶⁻⁸. As the number of biological targets with available 3D structures is limited, interaction-based approaches are less useful than interaction-free ones when faced with unknown protein-ligand complexes. In contrast, without relying on direct physical interactions, interaction-free approaches infer binding affinity from protein and ligand lower-dimensional data, such as amino acid sequence and simplified molecular input line entry system (SMILES) string⁹. Regarding PLA prediction as a regression task, interaction-free approaches first feed the protein and ligand inputs into different encoders such as convolutional neural network (CNN)^{10,11}, graph neural network (GNN)^{12,13}, and Transformer¹⁴⁻¹⁶.

With these advanced deep learning techniques, data-driven representations can be automatically learned from large-scale protein and ligand data. Subsequently, the binding affinities between proteins and ligands are predicted through a decoder that incorporates and processes their representations. Obviously, interaction-free methods have wider applications, as they take 1D or 2D structural information from proteins and ligands as input and thus have fewer restrictions on data.

Despite their promising results, existing interaction-free models still suffer from two key limitations: (1) their reliance solely on structural information creates performance bottlenecks, and (2) their predictions often lack scientific interpretability. To overcome these limitations, we argue that interaction-free models should incorporate biochemical factual knowledge during the encoding of proteins and ligands. Such knowledge provides rich external information that not only enhances predictive accuracy but also offers scientific grounding for interpretability. For proteins, Gene Ontology (GO)¹⁷ annotations describe their molecular functions, biological processes, and cellular components, which are highly relevant to protein-ligand binding. For instance, if a protein’s molecular function includes *ATP binding*, it may exhibit high affinity for ATP-like ligands. Involvement in biological processes such as *signal transduction* can suggest potential molecular interactions or pathway associations. Similarly, cellular component annotations like *cell membrane* can inform ligand accessibility. For ligands, knowledge can be derived from molecular descriptors and chemical features. Ligand properties (LP) such as the number of *hydrogen bond donors* (e.g., amino groups, phenolic hydroxyl groups) and *acceptors* (e.g., oxygen, nitrogen atoms) are crucial for forming hydrogen bonds with proteins. These interactions play a pivotal role in protein-ligand binding, making such properties essential for accurate PLA prediction.

However, integrating such domain knowledge presents two key challenges: (1) how to organize the diverse and complex knowledge into a form that the model can easily process, and (2) how to enable the model to sufficiently capture the organized knowledge. To address the first challenge, knowledge graphs (KGs)¹⁸ are expected to be the optimal solution due to their proven capabilities in knowledge tasks. KGs constructed from GO and LP can systematically describe biochemical knowledge of proteins and ligands via the form of *entity-relation-entity* triples. Correspondingly, KG embedding techniques¹⁹ can map proteins, ligands, and related entities into continuous vector spaces, preserving both semantic and relational information. For the second challenge, a straightforward approach is to directly use the KG-derived embeddings of proteins and ligands, alongside structural representations, for PLA prediction. However, this approach falls short for knowledge-sparse entities, as KG embeddings cannot substitute structural encoders when only amino acid sequences or SMILES strings are available. Therefore, incorporating the KG to enhance the structural information encoder is a more effective strategy that can offer the best of both worlds. To this end, we propose a joint learning framework that bridges structural encoding and KG embedding through multi-objective learning, ensuring that biochemical knowledge is effectively injected during the representation learning process.

In this paper, we propose a knowledge-enhanced protein-ligand binding affinity prediction (KEPLA) model, which is the first general framework to achieve deep integration of biochemical factual knowledge into the task of PLA prediction. The overall architecture of KEPLA follows an encoder-decoder paradigm. Specifically, it employs hybrid encoders—evolutionary sequence model (ESM)²⁰ for 1D amino acid sequences and graph convolutional networks (GCNs)²¹ for 2D molecular graphs—to generate both global and local representations of proteins and ligands. To ensure the encoders effectively capture and leverage biochemical knowledge for the task, KEPLA jointly trains the encoded protein and ligand representations on two objectives: KG embedding and PLA prediction. For the KG embedding objective, the encoded global representations are directly used as the entity embeddings of our constructed KG, which covers protein-GO and ligand-LP knowledge. Then they are optimized alongside other learnable entity and relation embeddings using standard KG embedding techniques. For the PLA prediction objective, the encoded local representations are processed by a pairwise interaction module, which uses a cross attention network²² to derive protein-ligand joint representations. The joint representations are then decoded by a multilayer perceptron (MLP) decoder to produce the final affinity prediction. By jointly minimizing the losses of both objectives, our model takes into account the relevant biochemical knowledge while making PLA predictions and thus can be enhanced. We conduct extensive experiments under both in-domain and cross-domain settings, comparing KEPLA with state-of-the-art methods. Results demonstrate that KEPLA achieves significant performance gains, improving RMSE metric by 5.28% and 12.42% on two benchmark datasets, respectively. Moreover, KEPLA provides more interpretable insights into the prediction through its knowledge-grounded framework.

To summarize, our contributions are as follows: (1) We propose KEPLA, the first knowledge-enhanced PLA predicting model that incorporates a KG with the interaction-free framework, achieving notable performance improvements. (2) By leveraging the KG and cross attention mechanism, KEPLA provides an interpretable prediction through relevant knowledge and attention visualization, moving beyond traditional black-box outputs. (3) We construct and release a novel KG dataset based on PDBbind, promoting the research on PLA prediction.

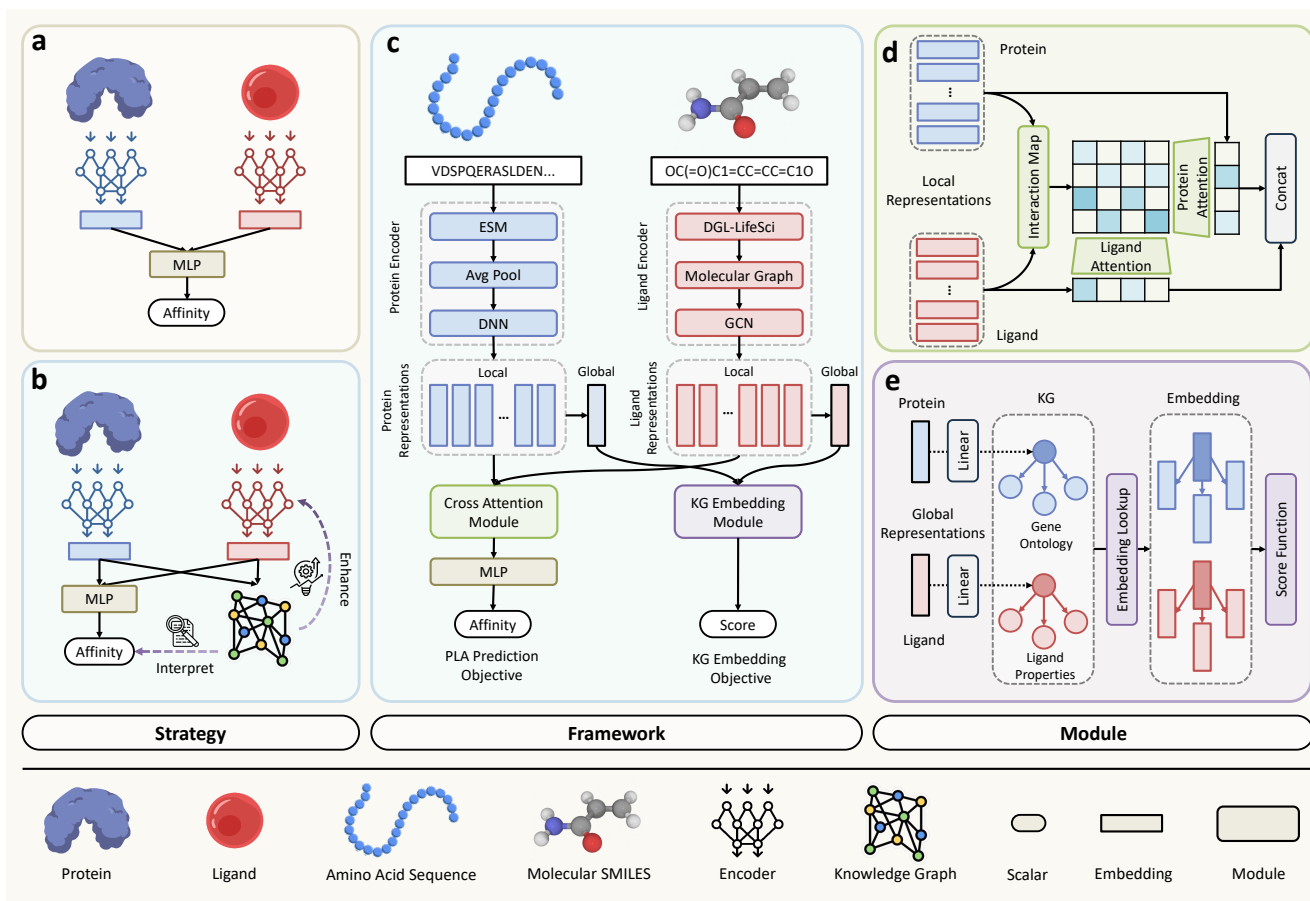


Figure 1. Overview of the KEPLA framework. (a) Strategy of existing PLA prediction models. (b) Strategy of our KEPLA model. The key difference lies in the incorporation of a biochemical KG, which enhances both protein and ligand encoding. (c) Detailed architecture of KEPLA. The model employs two separate encoders: an ESM-based encoder processes the amino acid sequence, and a GCN-based encoder handles the SMILES string. These generate both local and global representations for proteins and ligands. The global representations are used in the KG embedding module, while the local representations are input into a cross attention module for PLA prediction. (d) The cross attention module. Here, an interaction map is computed via the multiplication of protein and ligand local representations, which serves as a similarity matrix to derive cross attention. The cross attention enables fine-grained fusion of protein and ligand local representations, resulting in a joint representation. This joint representation is passed through an MLP decoder to predict binding affinity. (e) The KG embedding module. Here, linear transformations project the global protein and ligand representations into a semantic space. Combined with entity and relation embeddings from the KG, a score function evaluates the plausibility of triplets, which forms the objective of this module.

Results

Overview of KEPLA

The proposed KEPLA framework is illustrated in Figure 1. Given an input protein-ligand pair, we first encode the protein amino acid sequence and the ligand molecular graph separately using ESM and GCN blocks, respectively. To incorporate relevant biochemical knowledge into the representation learning process, the encoded representations are further embedded into a KG module and optimized with the KG embedding objective. Simultaneously, a cross attention module is employed to capture fine-grained interactions between the protein and ligand representations. This module includes a local interaction mapping step followed by a cross attention computation step, which together generate a joint protein-ligand representation. Finally, a fully connected MLP decoder produces a predictive score representing the binding affinity. Details of each module in the KEPLA model, along with the training procedure, are provided in the **Methods** section.

Evaluation strategies and metrics

We evaluate prediction performance on two public datasets, PDBbind²³ and CSAR-HiQ²⁴, using two distinct data split strategies to simulate in-domain and cross-domain scenarios. For in-domain evaluation, following²⁵, we use the *refined set* of PDBbind as the primary training data, as there is substantial overlap between the full *general set* and CSAR-HiQ dataset. We randomly split the protein-ligand complexes in the *refined set* into training and validation sets at a 9:1 ratio. For testing, we use the PDBbind *core set* and the CSAR-HiQ dataset after removing any overlapping complexes from the *refined set*. For cross-domain evaluation, we propose a clustering-based pair split strategy to simulate domain shift. We conduct cross-domain evaluation on the larger-scale PDBbind datasets. Specifically, we first use the single-linkage algorithm to cluster proteins and ligands by PSC (pseudo-amino acid composition)²⁶ and ECFP4 (extended connectivity fingerprint, up to four bonds)²⁷, respectively. After that, we randomly select 60% protein clusters and 60% ligand clusters from the clustering result, and consider all protein-ligand pairs between the selected ligands and proteins as source domain data. All the pairs between proteins and ligands in the remaining clusters are considered to be target domain data. Detailed clustering implementation is provided in the **Supplementary Information**. Under this split, source and target domains are disjoint and follow different distributions. In line with standard domain adaptation settings, we use all labeled source domain data and 80% of the unlabeled target domain data for training, where this 80% also serves as the validation set. The remaining 20% of labeled target data is used for testing. Compared to in-domain random splits, this cross-domain setup poses a greater challenge but better reflects real-world generalization scenarios in drug discovery.

To comprehensively evaluate the model performance, following^{28,29}, we adopt Root Mean Square Error (RMSE), Mean Absolute Error (MAE), Pearson's correlation coefficient (R), and the standard deviation (SD) in regression to measure the prediction error. Detailed descriptions of these metrics are provided in the **Supplementary Information**. For evaluation, lower RMSE, MAE, and SD values indicate better performance, whereas higher R values are preferable.

In-domain performance comparison

We compare KEPLA against a range of representative interaction-free and interaction-based baseline models under the random split setting. The interaction-free baselines include RF-Score²⁵, DeepDTA¹⁰, GraphDTA (including GCN, GAT, GIN, and GAT-GCN)³⁰, DrugBAN³¹. The interaction-based baselines include Pafnucy²⁸, OnionNet²⁹, SGCN³², GraphTrans³³, NL-GCN³⁴, GNN-DTI³⁵, DMPNN³⁶, MAT³⁷, DimeNet³⁸, CMPNN³⁹, SIGN⁴⁰, and GIANT⁴¹. All baseline models are implemented using the official source codes and are evaluated on the same training, validation, and test sets. The validation set is used to select the model checkpoint with the lowest RMSE for final testing. It is worth noting that some baselines are not originally developed for PLA prediction and have been adapted accordingly for a fair comparison. The detailed description and setup of the baselines can be found in the **Supplementary Information**.

Table 1 presents the quantitative results. We report the mean and standard deviation of four evaluation metrics across five independent runs. When comparing model categories, we observe that interaction-based models generally outperform interaction-free models, highlighting the advantage of incorporating 3D structural information and physical interactions in PLA prediction. Despite being an interaction-free method, our proposed KEPLA achieves the best performance across all experimental settings on both datasets, surpassing even all interaction-based baselines. Specifically, KEPLA improves RMSE by 5.28% on the PDBbind dataset and by 12.42% on the CSAR-HiQ dataset compared to the best-performing baseline GIANT. These results strongly support KEPLA's superior predictive capability. Considering KEPLA requires only the molecular graph of ligand compounds and primary sequences of target proteins as input like most interaction-free methods, the outstanding performance benefits from knowledge-enhanced representation learning and local interaction modeling.

Cross-domain performance comparison

In-domain prediction under a random split setting is relatively easier and holds limited practical significance. Therefore, we further investigate the more realistic and challenging task of cross-domain PLA prediction, where the training and test data follow different distributions. To simulate this scenario, we partition the original PDBbind dataset into source and target domains using the clustering-based pair split strategy. As a complementary evaluation, we also perform experiments using a cold pair split on the PDBbind dataset. Specifically, we randomly select 70% of the proteins and ligands and collect all associated protein-ligand pairs as the training set. The remaining 30% of proteins and ligands are used to form the validation and test sets in a 3:7 ratio. This cold pair split strategy ensures that none of the proteins or ligands in the test set have been seen during training, providing a stringent test of model generalization.

The performance evaluation on the PDBbind dataset under both clustering-based and cold pair split strategies is shown in Figure 2. It is important to note that these experiments are restricted to interaction-free methods, as structural interaction information is unavailable in the simulated cross-domain and cold scenarios. Compared to the earlier in-domain results, the performance of all interaction-free PLA models drops significantly as shown in Figure 2a. This decline is primarily attributed to the reduced information overlap between the training and test sets, as well as the absence of sufficiently similar proteins and

Table 1. In-domain performance comparison on the PDBbind and CSAR-HiQ datasets under random split (statistics over five independent runs)

Method		PDBbind core set			
		RMSE ↓	MAE ↓	SD ↓	R ↑
Interaction-free methods	RF-Score	1.446 (0.008)	1.161 (0.007)	1.335 (0.010)	0.789 (0.003)
	DeepDTA	1.639 (0.026)	1.315 (0.023)	1.689 (0.025)	0.718 (0.014)
	GCN	1.735 (0.034)	1.343 (0.037)	1.719 (0.027)	0.613 (0.016)
	GAT	1.765 (0.026)	1.354 (0.033)	1.740 (0.027)	0.601 (0.016)
	GIN	1.640 (0.044)	1.261 (0.044)	1.621 (0.036)	0.667 (0.018)
	GAT-GCN	1.562 (0.022)	1.191 (0.016)	1.558 (0.018)	0.697 (0.008)
	DrugBAN	1.378 (0.025)	1.102 (0.019)	1.328 (0.020)	0.788 (0.015)
Interaction-based methods	Pafnucy	1.585 (0.013)	1.284 (0.021)	1.563 (0.022)	0.695 (0.011)
	OnionNet	1.407 (0.034)	1.078 (0.028)	1.391 (0.038)	0.768 (0.014)
	SGCN	1.583 (0.033)	1.250 (0.036)	1.582 (0.320)	0.686 (0.015)
	GraphTrans	1.539 (0.044)	1.182 (0.046)	1.521 (0.042)	0.714 (0.019)
	NL-GCN	1.516 (0.019)	1.198 (0.013)	1.511 (0.024)	0.720 (0.010)
	GNN-DTI	1.492 (0.025)	1.192 (0.032)	1.471 (0.051)	0.736 (0.021)
	DMPNN	1.493 (0.016)	1.188 (0.009)	1.489 (0.014)	0.729 (0.006)
	MAT	1.457 (0.037)	1.154 (0.037)	1.445 (0.033)	0.747 (0.013)
	DimeNet	1.453 (0.027)	1.138 (0.026)	1.434 (0.023)	0.752 (0.010)
	CMPNN	1.408 (0.028)	1.117 (0.031)	1.399 (0.025)	0.765 (0.009)
	SIGN	1.316 (0.031)	1.027 (0.025)	1.312 (0.035)	0.797 (0.012)
GIANT	1.269 (0.020)	0.999 (0.018)	1.265 (0.024)	0.814 (0.008)	
Ours	KEPLA	1.202 (0.017)	0.936 (0.013)	1.195 (0.016)	0.832 (0.005)
Method		CSAR-HiQ set			
		RMSE ↓	MAE ↓	SD ↓	R ↑
Interaction-free methods	RF-Score	1.947 (0.012)	1.466 (0.009)	1.796 (0.020)	0.723 (0.007)
	DeepDTA	1.983 (0.036)	1.510 (0.059)	2.037 (0.051)	0.633 (0.036)
	GCN	2.324 (0.079)	1.732 (0.065)	2.302 (0.061)	0.464 (0.047)
	GAT	2.213 (0.053)	1.651 (0.061)	2.215 (0.050)	0.524 (0.032)
	GIN	2.158 (0.074)	1.624 (0.058)	2.156 (0.088)	0.558 (0.047)
	GAT-GCN	1.980 (0.055)	1.493 (0.046)	1.969 (0.057)	0.653 (0.026)
	DrugBAN	1.672 (0.034)	1.334 (0.042)	1.728 (0.059)	0.767 (0.039)
Interaction-based methods	Pafnucy	1.939 (0.103)	1.562 (0.094)	1.885 (0.071)	0.686 (0.027)
	OnionNet	1.927 (0.071)	1.471 (0.031)	1.877 (0.097)	0.690 (0.040)
	SGCN	1.902 (0.063)	1.472 (0.067)	1.891 (0.077)	0.686 (0.030)
	GraphTrans	1.950 (0.072)	1.508 (0.069)	1.886 (0.083)	0.687 (0.033)
	NL-GCN	1.840 (0.024)	1.393 (0.016)	1.817 (0.028)	0.716 (0.011)
	GNN-DTI	1.972 (0.061)	1.547 (0.058)	1.834 (0.090)	0.709 (0.035)
	DMPNN	1.886 (0.026)	1.488 (0.054)	1.865 (0.035)	0.697 (0.013)
	MAT	1.879 (0.065)	1.435 (0.058)	1.816 (0.083)	0.715 (0.030)
	DimeNet	1.805 (0.036)	1.338 (0.026)	1.798 (0.027)	0.723 (0.010)
	CMPNN	1.839 (0.096)	1.411 (0.064)	1.767 (0.103)	0.730 (0.052)
	SIGN	1.735 (0.031)	1.327 (0.040)	1.709 (0.044)	0.754 (0.014)
GIANT	1.666 (0.024)	1.242 (0.030)	1.633 (0.034)	0.779 (0.011)	
Ours	KEPLA	1.459 (0.019)	1.132 (0.026)	1.517 (0.032)	0.813 (0.012)

Results are reported as mean (standard deviation). For each dataset and metric, the best performance is highlighted in bold, and the second-best is underlined.

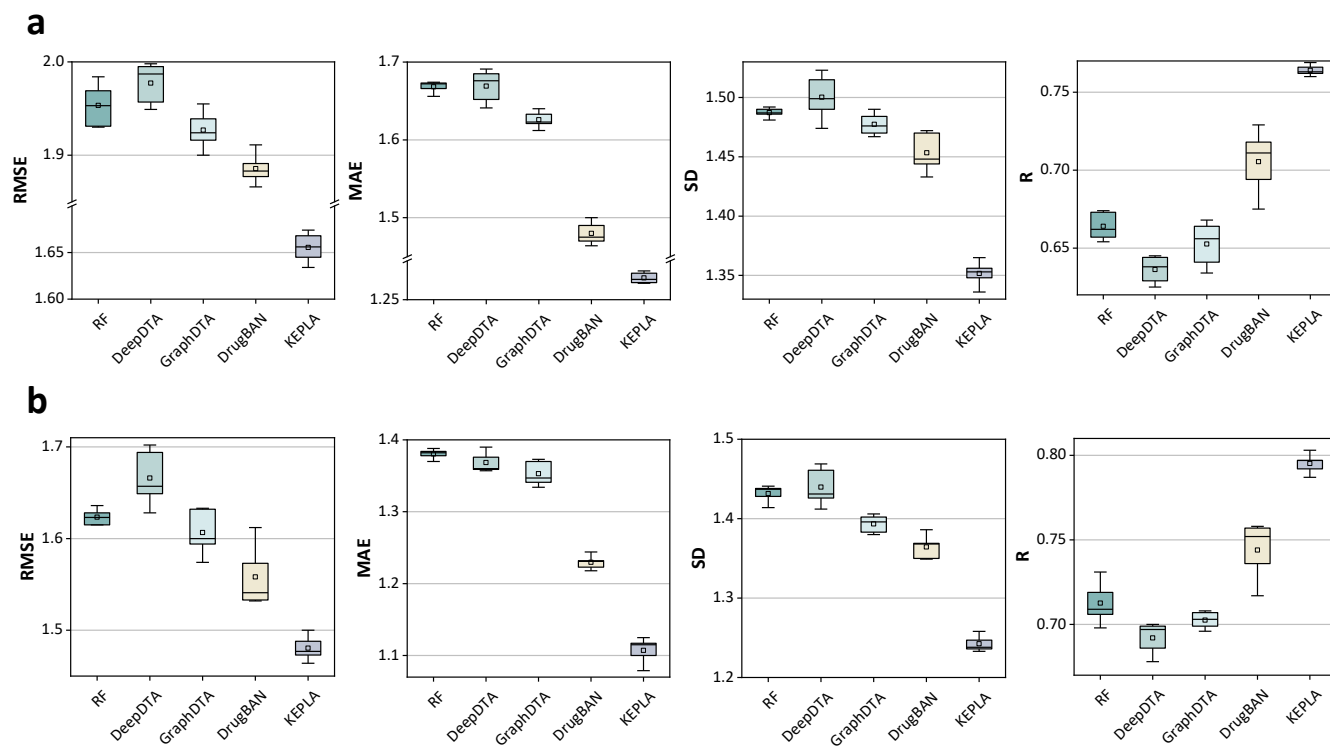


Figure 2. Cross-domain performance comparison on the PDBbind dataset (statistics over five independent runs). (a) Performance comparison of interaction-free methods under clustering-based pair split. **(b)** Performance comparison of interaction-free methods under cold pair split. The box plots display the median as the center line and the mean as a square marker. The minimum and lower percentile indicate the worst and second-worst scores, while the maximum and upper percentile represent the best and second-best scores, respectively.

ligands to serve as references. Moreover, Figure 2b highlights a noticeable performance drop when moving from random split to cold pair split, emphasizing that prediction accuracy on unseen test data cannot solely rely on previously encountered protein or ligand features.

Despite the increased difficulty of cross-domain and cold settings, KEPLA consistently outperforms all state-of-the-art deep learning baselines. Specifically, it achieves improvements of 12.25% in RMSE and 8.37% in R over DrugBAN on the PDBbind dataset. These results highlight the robustness of KEPLA and underscore its strong generalization capability across domains. Interestingly, the traditional RF-Score model also performs well, even consistently outperforming the deep learning baseline DeepDTA under cross-domain and cold settings. This observation suggests that deep learning approaches are not inherently superior to shallow machine learning models in challenging generalization scenarios. One possible explanation is that data-driven deep learning models are more sensitive to data bias and distribution shifts. Furthermore, we observe that KEPLA experiences a 36.55% performance drop compared to its random split performance, while DrugBAN shows a slightly higher average decline of 36.87%. This indicates that KEPLA’s knowledge-enhanced design contributes to greater robustness, and supports the notion that integrating external knowledge can effectively mitigate the impact of data bias in deep learning-based PLA prediction.

Ablation study

We conduct an ablation study to investigate the contributions of two key components in KEPLA: the KG and the cross attention modules. The results of various KEPLA variants are presented in Figure 3. To evaluate the impact of KG enhancement, we consider three variants of KEPLA with different configurations: KEPLA using only the protein-side KG, KEPLA using only the ligand-side KG, and KEPLA without KG enhancement. As shown in Figure 3a, the model’s strong performance is clearly supported by the incorporation of external knowledge, validating the effectiveness of KG enhancement. Notably, the protein-side KG contributes more significantly to affinity prediction than the ligand-side counterpart. A likely explanation is that the protein KG contains a greater number of entities and richer relational information, offering more comprehensive context for representation learning.

To further assess the effectiveness of the cross attention mechanism, we evaluate three KEPLA variants that differ in how

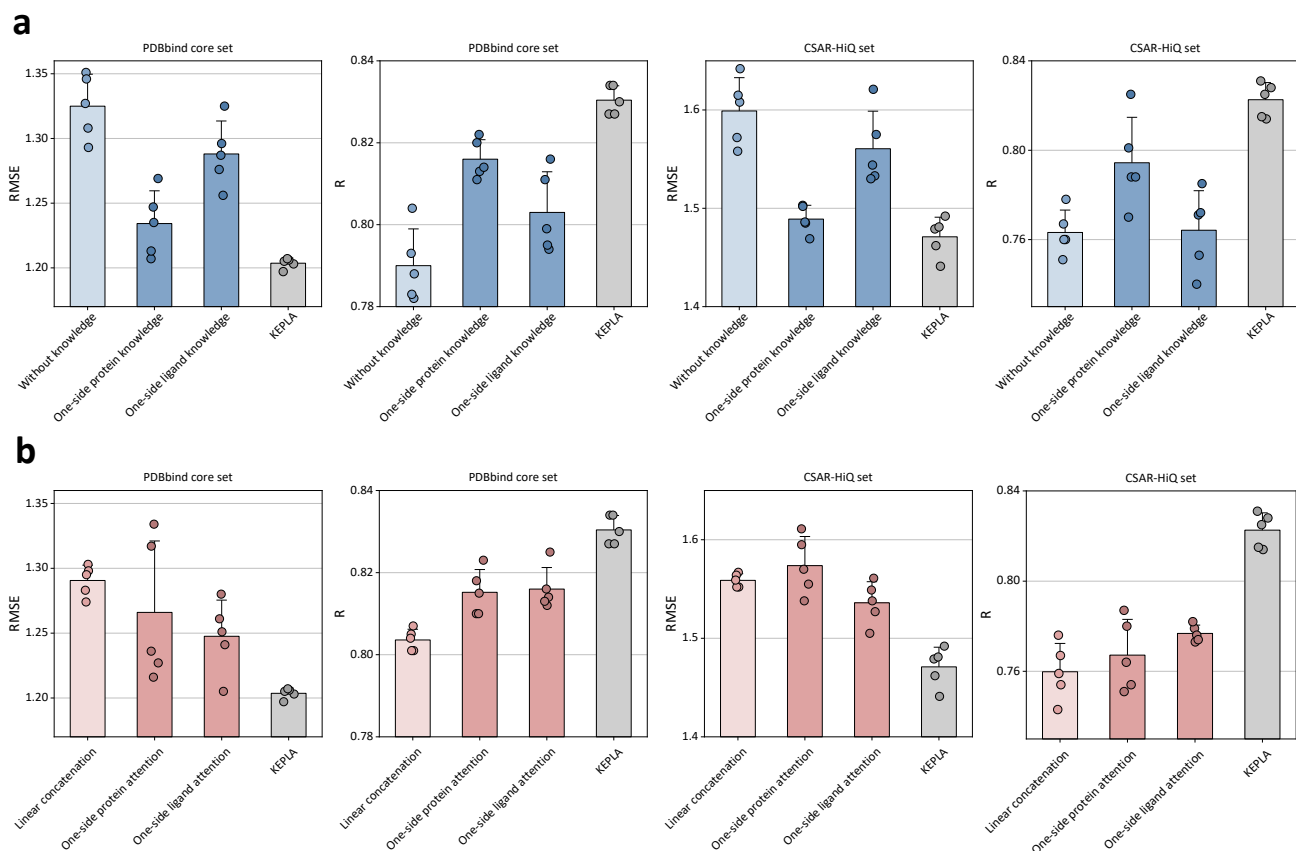


Figure 3. Ablation study in terms of RMSE and R on the PDBbind and CSAR-HiQ datasets under random split (statistics over five independent runs). (a) Performance of different variants of the KG module. (b) Performance of different variants of the cross attention module. The vertical bars represent the mean values, while the black lines denote standard deviations (error bars). Dots indicate the performance scores from each individual run.

they compute joint representations between proteins and ligands: one-side protein attention, one-side ligand attention, and linear concatenation. In these variants, the cross attention module in KEPLA is replaced with either ligand-side or protein-side attention. The one-side attention variants adopt the neural attention mechanism proposed in⁴², where the joint representation is derived from the interaction between a ligand vector and a protein fragment matrix. The linear concatenation variant, on the other hand, simply concatenates the protein and ligand vector representations following a max-pooling operation. As shown in Figure 3b, the results confirm that the cross attention mechanism is both effective and essential, as it enables the model to capture fine-grained interactions crucial for accurate PLA prediction. Among the one-side attention variants, ligand-side attention yields better performance. This may be attributed to the fact that ligand-side attention operates on local representations derived from the ligand’s 2D molecular structure, which tend to be more spatially precise compared to the 1D sequence-based representations of proteins.

Structural-level interpretability with cross attention

A further strength of KEPLA lies in its ability to provide interpretability at both structural and knowledge levels—an essential feature for drug design applications. Structural-level interpretability is achieved by leveraging cross attention weights to visualize the contribution of each substructure to the final prediction. To illustrate this, we examine three top-ranked predictions (PDB IDs: 3UI7⁴³, 2WTV⁴⁴, and 2QE4⁴⁵) corresponding to co-crystallized ligands from the Protein Data Bank (PDB)⁴⁶. Only X-ray structures with a resolution greater than 2.0Å and targeting human proteins are considered⁴⁷. Additionally, the selected complexes must exhibit binding affinities at the nanoscale and belong to the test set. Visualization results are presented in Figure 4a, alongside protein-ligand interaction maps derived from the corresponding X-ray structures. For each ligand, the top 20% of atoms, ranked by cross attention weights, are highlighted in orange.

For complex 3UI7 (pyrazoloquinoline bound to human PDE10A), the ligand molecule pyrazoloquinoline features a fused structure composed of a pyrazole ring and a quinoline ring. The pyrazole ring is a five-membered nitrogen-containing

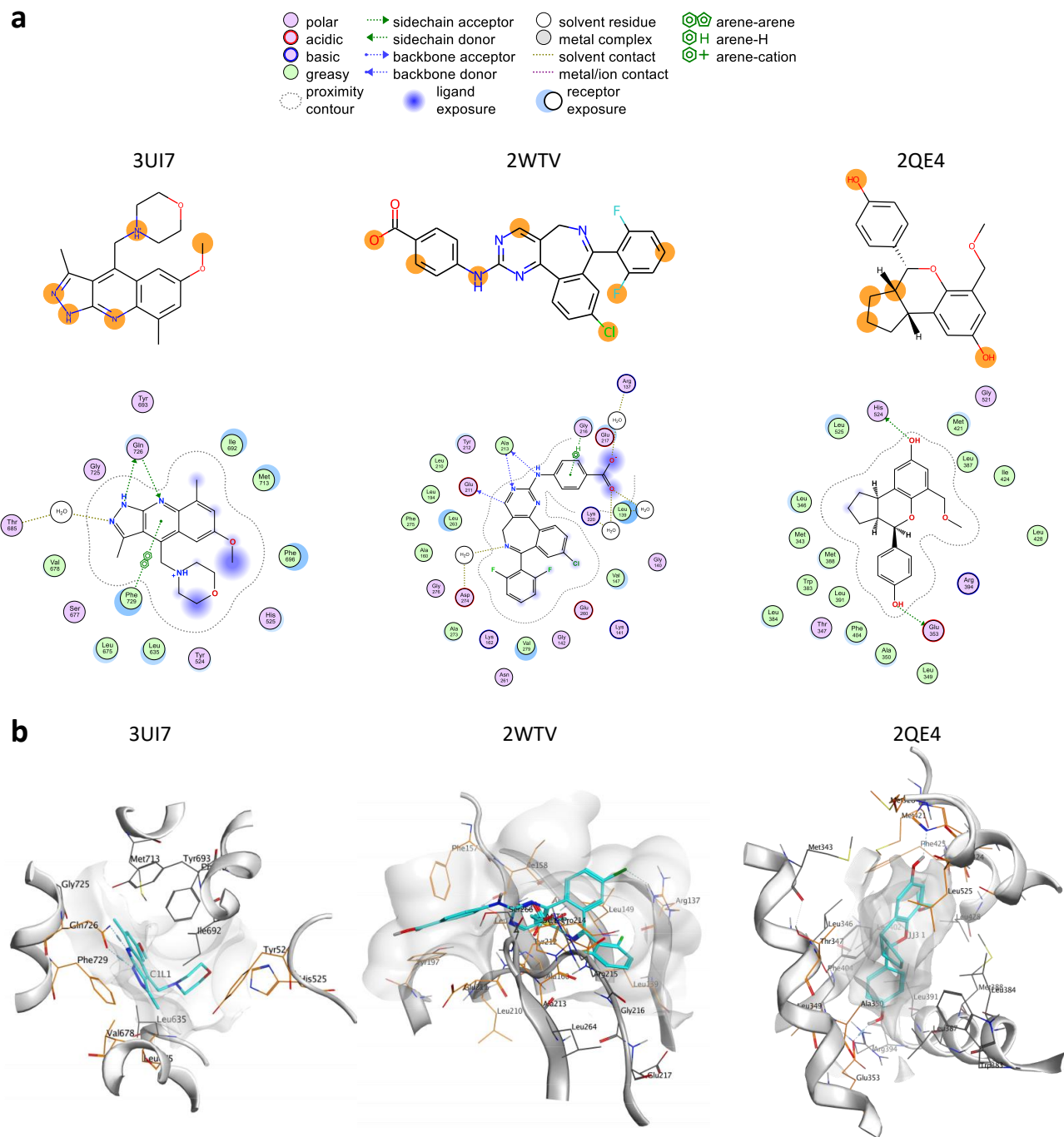


Figure 4. Visualization of ligands and binding pockets for structural-level interpretability study. (a) Interpretability of co-crystallized ligands. The upper section of each panel displays the 2D structures of ligands, with atoms highlighted in orange to indicate those predicted to contribute to protein binding. All 2D structures are visualized using RDKit. The lower section of each panel presents protein-ligand interaction maps derived from the corresponding crystal structures. (b) Interpretability of binding pocket structures. The 3D representations show protein-ligand binding pockets, with correctly predicted binding-site residues highlighted in orange and the corresponding ligands shown in cyan. Remaining amino acid residues, secondary structure elements, and surface maps are shown in grey. All protein-ligand interaction maps and 3D visualizations of X-ray crystal structures are generated using the Molecular Operating Environment (MOE) software.

heterocycle, while the quinoline ring consists of a pyridine ring fused with a benzene ring. Our model correctly identifies the nitrogen-containing heterocyclic region as critical for protein-ligand binding: the nitrogen atom bearing a hydrogen in the pyrazole ring acts as a hydrogen bond donor to the side chain of Gln729; the other nitrogen atom interacts with Thr685 via a solvent molecule; and the nitrogen atom in the pyridine ring serves as a hydrogen bond acceptor to Gln729. Conversely, the methoxy group on the benzene ring is incorrectly predicted to form specific interactions with the protein, despite being solvent-exposed, though this exposure may facilitate additional binding interactions (blue highlight). Additionally, the pyridine ring, which engages in an arene-arene interaction with Phe729, is partially emphasized by the interpretability model. Notably, although only five atoms of the ligand are among the top 20% atoms, most correspond to distinct protein-ligand interaction sites confirmed by the X-ray crystal structure.

In complex 2WTV (MLN8054 bound to human Aurora kinase A), the core scaffold of MLN8054 comprises a fused polycyclic structure connected to a difluorophenyl group and an anilino moiety, with chlorine and carboxylate substituents. The interpretability of our model effectively highlights key interaction patterns relevant to protein-ligand binding. For instance, within the aniline group, the amino group is correctly identified as forming a hydrogen bond with the backbone of Ala213 (acting as a donor), and the adjacent benzene ring is partially highlighted due to its arene-hydrogen interaction with Gly216. The carboxylate anion is also accurately identified, interacting with Tyr212 via a solvent-mediated contact. Furthermore, the nitrogen-containing aromatic heterocycle is recognized for its potential to act as either a hydrogen bond donor or acceptor, with one specific nitrogen atom explicitly highlighted for donating a hydrogen bond to the backbone of Glu211. The fluorine atoms in the difluorophenyl group and the chlorine substituent are also marked, likely due to their solvent exposure and potential role in enhancing binding affinity. Despite MLN8054 (in 2WTV) being considerably larger and more complex than pyrazoloquinoline (in 3UI7), the model demonstrates strong interpretability by accurately reflecting most of the key interactions confirmed by the crystal structure.

In complex 2QE4 (benzopyran agonist complexed with the human estrogen receptor), the ligand belongs to the class of organic compounds known as 6-hydroxyflavonoids—a subclass of flavonoids characterized by a hydroxyl group at the C-6 position of the flavonoid backbone. The ligand also features several distinctive substituents, including a 1-benzopyran ring, a 1-hydroxy-2-unsubstituted benzenoid moiety, and a 4'-hydroxyflavonoid fragment. Although only a small proportion of the ligand's atoms are directly involved in protein-ligand interactions, the model accurately identifies these key interaction sites. Notably, the two hydroxyl groups on the aromatic rings are correctly highlighted as forming hydrogen bonds with the receptor, acting as donors to the side chains of Glu353 and His524, respectively. Additionally, two carbon atoms on the five-membered ring are marked as solvent-exposed, suggesting a potential role in mediating further binding interactions.

Regarding the more challenging task of interpreting protein sequences, the results are less specific compared to those for ligands. This limitation arises from the model's design, where attention weights are computed and visualizations are generated based on protein fragments composed of multiple residues. While this design choice improves computational efficiency, it inevitably reduces interpretability at the residue level, as it does not explicitly resolve which specific residues within each fragment are responsible for binding. Nonetheless, several key amino acid residues involved in binding are correctly highlighted as shown in Figure 4b. For example, in complex 3UI7, residues Gln726 and Phe729, both forming specific interactions with the ligand, are accurately highlighted, along with additional pocket residues such as Tyr524, His525, Leu675, Ser677, and Val678. In complex 2WTV, our model correctly highlights Glu211 and Ala213, which participate directly in ligand binding, as well as several additional binding-site residues: Leu139, Gly140, Lys141, Gly142, Ala160, Leu194, Leu210, and Tyr212. In complex 2QE4, Glu353 and His524 are successfully highlighted as key hydrogen bond partners of the ligand, in addition to pocket-forming residues Thr347, Leu349, Ala350, Met421, Ile424, Gly521, and Leu525. Statistically, across the three complexes, nearly half of the binding-site residues are correctly identified by the model. These results suggest that fragment-level attention provides a promising foundation for interpretability. Incorporating residue-level attention mechanisms could further enhance the resolution and accuracy of protein-ligand interaction explanations. Moreover, if predictions are not constrained to be interaction-free, integrating 3D structural and local spatial information from the binding pocket may further improve interpretability.

In addition, since the interpretability provided by KEPLA is adaptively learned from the PLA data itself, it has the potential to uncover previously unexplored local interaction patterns. Such insights could assist drug developers in optimizing the binding properties of a given scaffold or in minimizing the off-target liabilities of a compound.

Knowledge-level interpretability with knowledge graph

Ablation studies have confirmed that incorporating external knowledge related to proteins and ligands significantly improves affinity prediction. Building on this, we further investigate whether such external knowledge can also enhance the interpretability of protein-ligand binding. To this end, we identify the entities most closely associated with the target protein and ligand and attempt to derive plausible explanations for their interaction based on these entities. Specifically, we utilize the learned embeddings of entities and relations from the KG and continue applying the scoring function to evaluate all triplets involving the

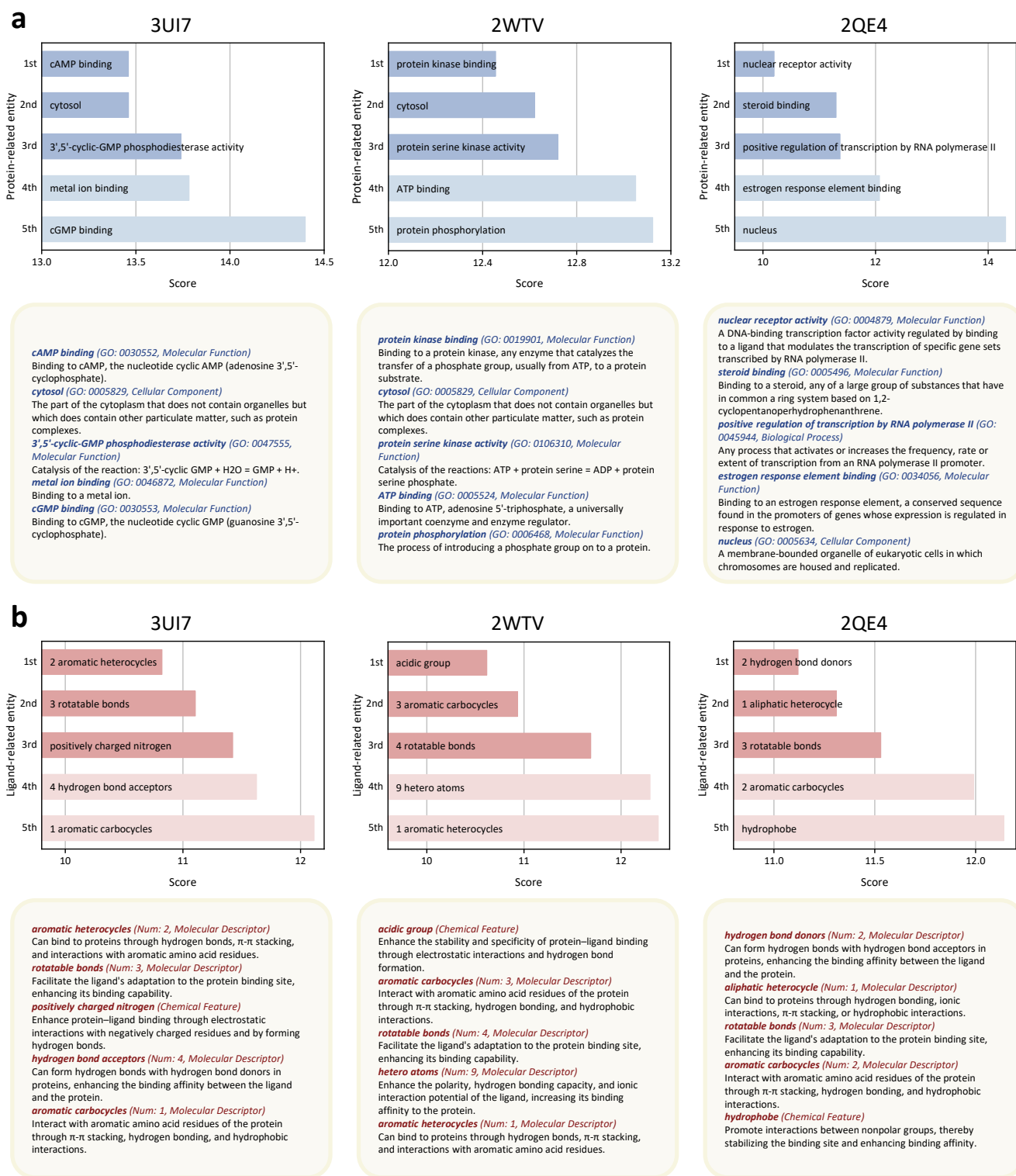


Figure 5. Biochemical knowledge of proteins and ligands for knowledge-level interpretability study. (a) Interpretability of protein biological knowledge. The upper part of each panel displays the GO entities most closely associated with the protein, ranked in ascending order according to their triplet scores from the KG embedding model. The lower part presents the types and detailed definitions of these entities, annotated with their corresponding GO IDs. **(b)** Interpretability of ligand chemical knowledge. The upper part of each panel shows the LP entities most closely related to the ligand, also ranked in ascending order by their triplet scores in the KG embedding model. The lower part provides the types and specific functions of these entities, with molecular descriptors annotated by their corresponding numbers.

target protein or ligand. A lower score indicates greater semantic proximity between the protein or ligand and the corresponding GO or LP entity. As shown in Figure 5, the top five closest entities are presented. These entities are considered the most relevant and are used, along with their definitions, to interpret the protein-ligand binding mechanism. To maintain consistency with prior experiments, we use the same case studies: PDB IDs 3UI7, 2WTV, and 2QE4.

For the PDB structure 3UI7 (pyrazoloquinoline bound to human PDE10A), the top GO entities most closely associated with the protein include *cAMP binding*, *cytosol*, *3',5'-cyclic-GMP phosphodiesterase activity*, *metal ion binding*, and *cGMP binding*. Definitions for these entities are provided in Figure 5a. Collectively, they suggest that PDE10A functions by catalyzing the hydrolysis of cAMP and cGMP in the cytosol, playing a role in intracellular signal transduction. This enzymatic activity is metal ion-dependent, specifically requiring coordination with Zn^{2+} and Mg^{2+} ions. The binding of the ligand pyrazoloquinoline to PDE10A is closely aligned with these biological functions. The ligand binds at the enzyme's catalytic domain, acting as a competitive inhibitor that blocks access to the natural substrates cAMP and cGMP, thereby preventing their hydrolysis. According to structural data from the PDB, Zn^{2+} and Mg^{2+} coordination sites in the catalytic pocket also participate in the protein-ligand interaction. On the ligand side, the top associated entities for pyrazoloquinoline are *two aromatic heterocycles*, *three rotatable bonds*, *positively charged nitrogen*, *four hydrogen bond acceptors*, and *one aromatic carbocycle*, with definitions provided in Figure 5b. These descriptors align well with the interpretability analysis shown in Figure 4a. Specifically, the presence of aromatic heterocycles suggests potential for π - π stacking or other aromatic interactions with residues such as Phe, along with hydrogen bonding and structural rigidity, factors known to positively influence binding affinity. Additionally, the ligand's rotatable bonds may contribute to conformational flexibility, enhancing its ability to adapt to the shape of the protein's binding pocket. Together, these findings help explain the strong binding affinity observed in complex 3UI7.

For the PDB structure 2WTV (MLN8054 bound to human Aurora kinase A), the top GO entities most closely associated with the protein include *protein kinase binding*, *cytosol*, *protein serine kinase activity*, *ATP binding*, and *protein phosphorylation*. These annotations indicate that Aurora kinase A plays a crucial role in spindle assembly and chromosome segregation during mitosis, primarily through its ATP-binding and serine/threonine kinase activities within the cytoplasm. The interaction between the ligand MLN8054 and Aurora kinase A is highly consistent with these functional annotations. MLN8054 is a selective inhibitor of Aurora kinase A that mimics ATP and competitively binds to its ATP-binding site. This binding inhibits the kinase's activity, suppressing phosphorylation of downstream substrate proteins and thereby disrupting cell division. On the ligand side, the LP entities most closely associated with MLN8054 include *acidic group*, *three aromatic carbocycles*, *four rotatable bonds*, *nine heteroatoms*, and *one aromatic heterocycle*. As shown in Figure 4a, the presence of heteroatoms facilitates hydrogen bonding and potential metal coordination, contributing to specific and high-affinity interactions with the protein. Aromatic heterocycles, commonly found in high-affinity drugs, are especially effective in optimizing molecular compatibility with binding pockets. Moreover, a greater number of rotatable bonds enhances the ligand's conformational flexibility, allowing it to better fit the shape of the binding site. Together, these molecular features help explain the strong binding affinity observed in the 2WTV complex.

For the PDB structure 2QE4 (benzopyran agonist complexed with the human estrogen receptor), the top GO entities most closely associated with the protein are *nuclear receptor activity*, *steroid binding*, *positive regulation of transcription by RNA polymerase II*, *estrogen response element binding*, and *nucleus*. Notably, steroid binding highlights the role of the estrogen receptor as a steroid hormone receptor that can be activated by benzopyran agonists exhibiting steroid-like structural features. The remaining GO annotations indicate that, upon activation, the estrogen receptor translocates into the nucleus, binds to specific DNA sequences known as estrogen response elements, and regulates the transcription of target genes involved in processes such as cell proliferation and differentiation. On the ligand side, the most relevant LP entities for the benzopyran agonist in 2QE4 include *two hydrogen bond donors*, *one aliphatic heterocycle*, *three rotatable bonds*, *two aromatic carbocycles*, and *hydrophobe*. Among these, the feature of two hydrogen bond donors is consistent with the interaction profile shown in Figure 4a. Hydrophobicity is also a critical factor in protein-ligand binding, as it promotes favorable interactions between nonpolar groups, contributing to the stabilization of the binding site and enhancing overall binding affinity. The implications of the remaining features have been discussed in the earlier examples and similarly contribute to binding specificity and adaptability.

The above examples demonstrate that the KEPLA model can effectively retrieve knowledge entities associated with both the protein and the ligand through KG, thereby leveraging biologically and chemically grounded textual knowledge to explain their binding interactions. Compared to purely data-driven black-box predictions, this knowledge-based interpretability can provide a more tangible and trustworthy foundation for rational drug discovery.

Discussion

In this work, we present KEPLA, an end-to-end knowledge-enhanced deep learning framework for protein-ligand binding affinity (PLA) prediction, designed to address the performance bottlenecks and limited interpretability of existing methods. Specifically, we construct a biochemical KG for proteins and ligands, respectively. The encoded representations of proteins and

ligands are integrated into the KG embedding objective to capture the rich semantic information within KG. Subsequently, the model employs cross attention mechanisms to perform fine-grained aggregation of the knowledge-enhanced representations, which are then fed into a decoder to predict binding affinity. We conduct extensive experiments to evaluate the effectiveness of KEPLA in addressing the performance and interpretability challenges.

To assess the predictive performance of our model, we compare KEPLA against several state-of-the-art baselines (spanning both interaction-free and interaction-based methods) on two widely used public datasets. Our experimental setup includes both a random split to assess in-domain performance and a cluster-based split to assess cross-domain generalization. Compared to state-of-the-art baselines, KEPLA consistently achieves superior PLA prediction accuracy under both settings. Notably, despite being an interaction-free model, KEPLA outperforms many interaction-based methods in the in-domain setting and maintains robust performance in the more challenging cross-domain scenario. Ablation study further confirms the critical role of KG in enhancing model performance. These findings suggest that incorporating external domain knowledge not only improves prediction accuracy but also mitigates the hidden data bias inherent in purely data-driven approaches.

To evaluate the interpretability of our model, we conduct case studies that leverage both the cross attention and KG modules to provide explanations from structural and knowledge-based perspectives. By mapping attention weights to protein fragments and ligand atoms, KEPLA can highlight interacting regions such as the protein binding pocket and ligand interacting atoms, offering structural insights into the predicted interactions. Furthermore, by linking proteins and ligands to GO and LP entities in the KG, KEPLA grounds predictions in biochemical context, thereby enhancing interpretability from a knowledge-driven perspective.

This work focuses on interaction-free PLA prediction using 1D protein sequences and 2D molecular graphs as input. Given that high-quality 3D protein structures are available for only a limited subset of known sequences, we deliberately refrain from incorporating 3D structural information in this study. However, recent breakthroughs, such as AlphaFold by DeepMind^{48,49}, which has predicted over 2 billion protein structures across a million species, present compelling opportunities for integrating 3D structural information into future chemogenomics-based PLA models. Inspired by principles of pairwise local interaction learning and domain adaptation, we anticipate that extending our approach to include 3D structures could further enhance both predictive performance and model interpretability. Furthermore, our current KG construction is grounded in basic biochemical knowledge. Expanding this to incorporate richer domain-specific and cross-disciplinary knowledge offers a promising direction for future improvement. Finally, the KEPLA framework is highly generalizable and can be readily adapted to other molecular interaction prediction tasks, including drug-drug interaction⁵⁰ and protein-protein interaction⁵¹.

Methods

Problem formulation

In PLA prediction, the goal is to estimate the binding strength between a target protein and a ligand compound. We represent each protein sequence as $\mathcal{P} = (a_1, a_2, \dots, a_K)$, where each a_i denotes one of the 23 amino acids. For the ligand compound, most existing deep learning approaches use the SMILES⁹, a 1D string format that encodes atoms and bond information in a molecule. While SMILES facilitates the use of classical deep learning approaches, its linear format does not naturally capture molecular structures, potentially leading to the loss of crucial spatial information and reduced predictive accuracy. To address this, our model converts each SMILES string into a corresponding 2D molecular graph. Formally, a ligand is represented as a graph $\mathcal{G} = (\mathcal{V}, \mathcal{E})$, where \mathcal{V} is the set of nodes (atoms), and \mathcal{E} is the set of edges (chemical bonds)⁵². Given a protein sequence \mathcal{P} and a ligand graph \mathcal{G} , the PLA prediction task aims to learn a model \mathcal{M} that maps the joint representation space $\mathcal{P} \times \mathcal{G}$ to a continuous binding affinity value $y \in \mathbb{R}$. The commonly used notations in this paper are summarized in the **Supplementary Information**.

Overall architecture

As a PLA prediction model, KEPLA consists of four main components: (1) ESM-based protein sequence encoding for learning protein representations; (2) GCN-based molecular graph encoding for learning ligand representations; (3) KG embedding objective, enhancing representations through external biochemical KG; (4) PLA prediction objective, enabling fine-grained modeling of protein-ligand interactions via cross attention. Subsequently, we present a detailed elucidation of these components.

Protein sequence encoding

The protein encoder is built upon the pre-trained ESM model²⁰, augmented with a multi-layer neural network. It transforms an input amino acid sequence into a set of latent vectors, each representing a local fragment of the protein. ESM, a widely recognized protein language model, has demonstrated strong performance in predicting protein structure, function, and other properties from individual sequences. To fully leverage ESM’s powerful encoding capabilities, we use it as the backbone of our protein encoder. Given a target protein sequence \mathcal{P} , we input it into the pre-trained ESM model and extract the final hidden

state as the initial feature matrix:

$$\mathbf{M}_p = \text{ESM}(\mathcal{P}), \quad (1)$$

where $\mathbf{M}_p \in \mathbb{R}^{D_p \times K}$, with D_p denoting the output dimension of ESM and K representing the maximum allowed sequence length. To support batch training, protein sequences longer than K are truncated, while shorter ones are zero-padded.

Since the initial features are high-dimensional and task-agnostic, they require further processing. To compress the representation and retain local sequence information, we apply average pooling over non-overlapping fragments of size s , yielding s -mer residue-level features:

$$\mathbf{X}_p = \text{AvgPool}_s(\mathbf{M}_p), \quad (2)$$

where $\mathbf{X}_p \in \mathbb{R}^{D_p \times M}$, with $M = K/s$ denoting the number of local fragments. Next, a multi-layer deep neural network (DNN) is employed to adapt these features to our task and extract higher-level abstractions of local protein fragments. The encoding process is defined as:

$$\mathbf{H}_p^{(l+1)} = \sigma(\text{DNN}(\mathbf{W}_n^{(l)}, \mathbf{b}_n^{(l)}, \mathbf{H}_p^{(l)})), \quad (3)$$

where $\mathbf{W}_n^{(l)}$ and $\mathbf{b}_n^{(l)}$ are the learnable weights and biases of the l -th DNN layer, $\mathbf{H}_p^{(l)}$ is the l -th hidden protein representation, and $\sigma(\cdot)$ is a non-linear activation function (ReLU in our case). The initial input is set as $\mathbf{H}_p^{(0)} = \mathbf{X}_p$. The final output, $\mathbf{H}_p \in \mathbb{R}^{D \times M}$, is adopted as the protein representation, where D is the representation dimension.

Molecular graph encoding

For each ligand compound, we convert its SMILES string into a 2D molecular graph \mathcal{G} . To represent the node (atom) information in \mathcal{G} , we initialize each atom using its chemical properties, following the implementation in the DGL-LifeSci library⁵³. Each atom is initially represented as a 74-dimensional integer vector describing eight pieces of information: atom type, degree, number of implicit hydrogens, formal charge, number of radical electrons, hybridization state, number of total hydrogen atoms, and aromaticity. This initialization is formally written as:

$$\mathbf{M}_d = \text{DGL-LifeSci}(\mathcal{G}), \quad (4)$$

resulting in the initial node feature matrix $\mathbf{M}_d \in \mathbb{R}^{74 \times N}$, where N is the maximum allowed number of atoms per molecule. Molecules with fewer atoms are padded with virtual nodes filled with zeros to ensure consistent dimensions for batch training. Next, a linear transformation is applied to project the integer feature matrix into a real-valued one:

$$\mathbf{X}_d = \mathbf{W}\mathbf{M}_d, \quad (5)$$

producing a dense feature matrix $\mathbf{X}_d \in \mathbb{R}^{D_d \times N}$, with D_d denoting the feature dimension.

To learn expressive representations of ligand molecules, we employ a multi-layer GCN block. GCN extends convolution operations to irregular graph structures by updating each node’s representation through aggregation of its neighboring nodes, effectively capturing molecular substructure information. We retain node-level representations to enable subsequent fine-grained modeling of interactions with protein fragments. The GCN-based ligand encoder is formulated as:

$$\mathbf{H}_d^{(l+1)} = \sigma(\text{GCN}(\mathbf{A}, \mathbf{W}_g^{(l)}, \mathbf{b}_g^{(l)}, \mathbf{H}_d^{(l)})), \quad (6)$$

where $\mathbf{W}_g^{(l)}$ and $\mathbf{b}_g^{(l)}$ are the learnable weight matrix and bias vector of the l -th GCN layer, $\mathbf{H}_d^{(l)}$ is the l -th hidden node representation, \mathbf{A} is the adjacency matrix of the graph \mathcal{G} (augmented with self-loops), and $\sigma(\cdot)$ denotes a non-linear activation function (ReLU in our case). The input to the first layer is set as $\mathbf{H}_d^{(0)} = \mathbf{X}_d$. The final output, $\mathbf{H}_d \in \mathbb{R}^{D \times N}$, is adopted as the ligand representation.

KG embedding objective

Thus far, the two encoders described above only capture the 1D and 2D structural information of proteins and ligands, respectively. To further enhance these encoders with biochemical factual knowledge, we integrate their outputs into a KG embedding framework. Specifically, we treat the encoded protein and ligand representations as entity embeddings within our constructed KG and incorporate them into a joint learning process alongside other entities and relations. The remainder of this subsection details our implementation.

Our KG structurally consists of *entity-relation-entity* triplets to describe relational knowledge. We define a triplet as (h, r, t) , where h and t are head and tail entities, and r is the relation linking them, whose type is usually predefined by the schema. This KG is composed of two distinct subgraphs: one centered around proteins and the other around ligands.

- **Protein KG (GO-based):** This subgraph incorporates two types of entities: protein entities $e_{protein}$ involved in the affinity prediction task, and Gene Ontology (GO) entities e_{GO} describing functional annotations. The GO entities cover three categories: Molecular Function (MF), Cellular Component (CC), and Biological Process (BP). Therefore, the protein-related triplets fall into three groups: *protein-MF*, *protein-CC*, and *protein-BP*.
- **Ligand KG (LP-based):** Similarly, this subgraph includes ligand entities e_{ligand} and ligand property (LP) entities e_{LP} . The LP entities are further divided into Molecular Descriptors (MD), i.e., numerical attributes derived from molecular structures (e.g., counts of hydrogen bond donors/acceptors), and Chemical Features (CF), which denote qualitative attributes (e.g., hydrophobe, positively charged). Accordingly, the ligand-related triplets fall into two groups: *ligand-MD* and *ligand-CF*.

Next, we involve the protein and ligand representations in the KG embedding objective to enhance the protein and ligand encoding with external knowledge. Since the encoders yield matrix-form local representations unsuitable for KG embeddings, we first compute vector-form global representations by averaging across the local representations, then project them into the KG embedding space via a linear transformation:

$$\mathbf{h}_p = \mathbf{W}_k^1 \text{Average}(\mathbf{H}_p) + \mathbf{b}_k^1, \quad \mathbf{h}_d = \mathbf{W}_k^2 \text{Average}(\mathbf{H}_d) + \mathbf{b}_k^2, \quad (7)$$

where $\text{Average}(\cdot)$ denotes the averaging operation over all local representations. \mathbf{W}_k^* and \mathbf{b}_k^* are learnable weight matrices and bias vectors that map the global representations into the KG embedding space. The resulting \mathbf{h}_p and $\mathbf{h}_d \in \mathbb{R}^D$ serve as the semantic embeddings of the protein and ligand entities in the KG. Similar to⁵⁴, the embedding sets of other entities and relations are denoted by learnable $\mathbf{T} \in \mathbb{R}^{D \times T}$ and $\mathbf{R} \in \mathbb{R}^{D \times R}$, where T is the number of non-protein and non-ligand entities, and R is the number of relation types.

To achieve the KG embedding objective, we train the KG by optimizing the corresponding embeddings to fit the triplet relations. The objective function is defined as:

$$\mathcal{L}_{KGE} = \frac{1}{|\mathcal{S}|} \sum_{(h,r,t) \in \mathcal{S}} F(h,r,t), \quad (8)$$

where \mathcal{S} is the set of all KG triplets, and (h,r,t) is one of the triplets. $F(\cdot)$ is the score function of the KG embedding model. For modeling protein and ligand subgraphs, we adopt two widely used KG embedding models. RotatE⁵⁵ for the protein-GO subgraph:

$$F_p(h,r,t) = \|\mathbf{h} \circ \mathbf{r} - \mathbf{t}\|, \quad (9)$$

where \circ denotes the Hadamard (element-wise) product. TransE⁵⁴ for the ligand-LP subgraph:

$$F_d(h,r,t) = \|\mathbf{h} + \mathbf{r} - \mathbf{t}\|. \quad (10)$$

In both functions, \mathbf{h} is the embedding of the head entity, which is always a protein or ligand entity, and \mathbf{t} is the embedding of the tail entity, which is always a GO or LP entity. \mathbf{r} denotes the embedding of the relation between the head and the tail entities.

PLA prediction objective

In parallel with KG embedding, we employ a cross attention module to capture fine-grained, pairwise local interactions between protein and ligand substructures. This module comprises two main steps: (1) constructing an interaction map to measure substructure-level similarity, and (2) applying cross attention to derive a joint protein-ligand representation.

For the first step, ESM and GCN encoders have already generated hidden representations for protein and ligand: $\mathbf{H}_p = \{\mathbf{h}_p^1, \mathbf{h}_p^2, \dots, \mathbf{h}_p^M\}$ and $\mathbf{H}_d = \{\mathbf{h}_d^1, \mathbf{h}_d^2, \dots, \mathbf{h}_d^N\}$, where M and N are the number of fragments in a protein and the number of atoms in a ligand, respectively. Using these hidden representations, we construct a pairwise interaction matrix $\mathbf{V} \in \mathbb{R}^{M \times N}$:

$$\mathbf{V} = \mathbf{H}_p^\top \mathbf{H}_d. \quad (11)$$

Each element in \mathbf{V} reflects the interaction strength between a specific protein fragment and a ligand atom, thus identifying potential binding regions.

To extract a joint representation informed by these local interactions, we treat the interaction matrix as a similarity matrix and compute cross attention weights over both protein and ligand substructures. Protein attention $\alpha_p \in \mathbb{R}^M$ is calculated by summing the interactions across all ligand atoms and normalizing via a Softmax function:

$$\alpha_p = \text{Softmax}\left(\frac{1}{\sqrt{D}} \cdot \sigma\left(\frac{1}{N} \cdot \text{Sum}(\mathbf{V})\right)\right), \quad (12)$$

where $\text{Sum}(\cdot)$ denotes column-wise summation in matrix \mathbf{V} , and the result accumulates each fragment’s interactions across ligand atoms. $\sigma(\cdot)$ selects the Tanh function, and the $\text{Softmax}(\cdot)$ normalizes the attention scores into a probability distribution. The scaling factor \sqrt{D} helps stabilize gradients. Ligand attention $\alpha_d \in \mathbb{R}^N$ is computed analogously by transposing the interaction matrix and aggregating over protein fragments:

$$\alpha_d = \text{Softmax}\left(\frac{1}{\sqrt{D}} \cdot \sigma\left(\frac{1}{M} \cdot \text{Sum}(\mathbf{V}^\top)\right)\right). \quad (13)$$

These attention weights can provide interpretability by highlighting which protein and ligand substructures contribute most to the interaction.

Using the attention weights, we compute the weighted sum of protein and ligand local representations and concatenate them to form a joint representation:

$$\mathbf{f}_{p,d} = \mathbf{H}_p \cdot \alpha_p \oplus \mathbf{H}_d \cdot \alpha_d, \quad (14)$$

where $\mathbf{f}_{p,d} \in \mathbb{R}^{2D}$ is the joint protein-ligand representation, and \oplus denotes vector concatenation. We feed this joint representation into an MLP decoder to predict the binding affinity:

$$\hat{y}_{p,d} = \text{MLP}(\mathbf{f}_{p,d}), \quad (15)$$

where each single layer consists of its own learnable weight matrix and bias vector, followed by a ReLU activation function. The PLA objective is defined as the mean absolute error between the predicted and true binding affinities:

$$\mathcal{L}_{PLA} = \frac{1}{|\mathcal{O}|} \sum_{(p,d) \in \mathcal{O}} |y_{p,d} - \hat{y}_{p,d}|, \quad (16)$$

where \mathcal{O} is the set of protein-ligand training pairs, and $y_{p,d}$ is the ground truth affinity.

To jointly learn structural and semantic knowledge, we combine the affinity prediction objective with the KG embedding objective. The overall training loss function to minimize is as follows:

$$\mathcal{L} = \mathcal{L}_{PLA} + \beta \mathcal{L}_{KGE} + \lambda \|\Theta\|_2^2, \quad (17)$$

where Θ denotes the set of all learnable parameters, β is a trade-off hyperparameter between tasks, and λ is the L_2 regularization coefficient. We use mini-batch Adam optimization⁵⁶ to train the model. For each mini-batch of sampled pairs $(p,d) \in \mathcal{O}$, we select the associated KG triplets, construct their representations, and update all model parameters via backpropagation using the gradient of the total loss.

Datasets

We evaluate KEPLA and baselines using the following publicly available benchmark datasets for PLA prediction. PDBbind is a widely used dataset that provides multi-dimensional binding structures of protein-ligand complexes along with experimentally determined binding affinities. In our experiments, we primarily use PDBbind v2016, which is the most frequently adopted version in recent studies. This version consists of three overlapping subsets: The *general set*, containing all 13,283 protein-ligand complexes; The *refined set*, comprising 4,057 higher-quality complexes selected from the general set; The *core set*, including 290 top-quality complexes curated through a rigorous selection process, serving as a benchmark for testing. For convenience, we refer to the 3,767 complexes that belong to the *refined set* but are not in the *core set* as the *refined set* in this paper. To further assess generalization ability, we additionally evaluate on the CSAR-HiQ dataset, an external benchmark consisting of two subsets with 176 and 167 protein-ligand complexes, respectively, sourced independently from PDBbind.

Implementation

KEPLA is implemented using Python 3.10 and PyTorch 2.1.2⁵⁷, along with functionalities from several auxiliary libraries, including DGL 2.4.0⁵⁸, DGL-LifeSci 0.3.2⁵³, Scikit-learn 1.5.2⁵⁹, NumPy 1.24.3⁶⁰, Pandas 2.2.2⁶¹, and RDKit 2024.03.5⁶². The protein encoder includes a pre-trained ESM2_t36_3B model, followed by two fully connected layers with dimensions [2560, 512, 128]. The average pooling window size is set to 9. The ligand encoder consists of three GCN layers with hidden dimensions of [128, 128, 128]. We cap the maximum allowed protein sequence length at 1,080 and the maximum number of ligand atoms at 290. In the cross attention module, we use a single attention head for simplicity. The latent embedding size is set to 128, and the fully connected decoder contains 512 hidden units. We set the batch size to 64 and optimize the model using the Adam optimizer with a learning rate of 1e-4. All models are trained for a maximum of 200 epochs, and the checkpoint with the lowest validation RMSE is selected for final evaluation on the test set.

Data availability

The experimental data used in this work are available at <https://github.com/hanliu95/KEPLA/tree/main/datasets>. All data used in this work are from public resources. The PDBbind dataset can be found at <https://www.pdbbind-plus.org.cn> and the CSAR-HiQ dataset can be found at <http://www.csardock.org>. The co-crystallized ligands from PDB are available at <https://www.rcsb.org> by searching their PDB IDs.

Code availability

The source code and implementation details of KEPLA are freely available at the GitHub repository (<https://github.com/hanliu95/KEPLA>).

References

1. Volkov, M. *et al.* On the frustration to predict binding affinities from protein–ligand structures with deep neural networks. *J. Medicinal Chem.* **65**, 7946–7958 (2022).
2. Haylett, D. G. Direct measurement of drug binding to receptors. *Textb. Recept. Pharmacol.* 153–182 (2003).
3. Sadybekov, A. V. & Katritch, V. Computational approaches streamlining drug discovery. *Nature* **616**, 673–685 (2023).
4. Luo, Y. *et al.* A network integration approach for drug-target interaction prediction and computational drug repositioning from heterogeneous information. *Nat. Commun.* **8**, 573 (2017).
5. Rezaei, M. A., Li, Y., Wu, D., Li, X. & Li, C. Deep learning in drug design: protein-ligand binding affinity prediction. *IEEE/ACM Transactions on Comput. Biol. Bioinforma.* **19**, 407–417 (2020).
6. Li, Y. *et al.* Dyscore: a boosting scoring method with dynamic properties for identifying true binders and nonbinders in structure-based drug discovery. *J. Chem. Inf. Model.* **62**, 5550–5567 (2022).
7. Li, M., Cao, Y., Liu, X. & Ji, H. Knowledge-enhanced and structure-enhanced representation learning for protein-ligand binding affinity prediction. *Pattern Recognit.* **166**, 111701 (2025).
8. Lai, H. *et al.* Interformer: an interaction-aware model for protein-ligand docking and affinity prediction. *Nat. Commun.* **15**, 10223 (2024).
9. Weininger, D. Smiles, a chemical language and information system. 1. introduction to methodology and encoding rules. *J. Chem. Inf. Comput. Sci.* **28**, 31–36 (1988).
10. Öztürk, H., Özgür, A. & Ozkirimli, E. Deepdta: deep drug–target binding affinity prediction. *Bioinformatics* **34**, i821–i829 (2018).
11. Lee, I., Keum, J. & Nam, H. Deepconv-dti: Prediction of drug-target interactions via deep learning with convolution on protein sequences. *PLoS Comput. Biol.* **15**, 1–21 (2019).
12. Hinnerichs, T. & Hoehndorf, R. Dti-voodoo: machine learning over interaction networks and ontology-based background knowledge predicts drug–target interactions. *Bioinformatics* **37**, 4835–4843 (2021).
13. Yang, Z., Zhong, W., Zhao, L. & Chen, C. Y.-C. Mgraphdta: deep multiscale graph neural network for explainable drug–target binding affinity prediction. *Chem. Sci.* **13**, 816–833 (2022).
14. Vaswani, A. *et al.* Attention is all you need. *Int. Conf. on Neural Inf. Process. Syst.* 1–11 (2017).
15. Chen, L. *et al.* Transformerpci: improving compound–protein interaction prediction by sequence-based deep learning with self-attention mechanism and label reversal experiments. *Bioinformatics* **36**, 4406–4414 (2020).
16. Huang, K., Xiao, C., Glass, L. M. & Sun, J. Moltrans: molecular interaction transformer for drug–target interaction prediction. *Bioinformatics* **37**, 830–836 (2021).
17. Ashburner, M. *et al.* Gene ontology: tool for the unification of biology. *Nat. Genet.* **25**, 25–29 (2000).
18. Ye, Q. *et al.* A unified drug–target interaction prediction framework based on knowledge graph and recommendation system. *Nat. Commun.* **12**, 6775 (2021).
19. Wang, Q., Mao, Z., Wang, B. & Guo, L. Knowledge graph embedding: A survey of approaches and applications. *IEEE Transactions on Knowl. Data Eng.* **29**, 2724–2743 (2017).
20. Lin, Z. *et al.* Evolutionary-scale prediction of atomic-level protein structure with a language model. *Science* **379**, 1123–1130 (2023).

21. Mastropietro, A., Pasculli, G. & Bajorath, J. Learning characteristics of graph neural networks predicting protein–ligand affinities. *Nat. Mach. Intell.* **5**, 1427–1436 (2023).
22. Hou, R., Chang, H., Ma, B., Shan, S. & Chen, X. Cross attention network for few-shot classification. *Int. Conf. on Neural Inf. Process. Syst.* 4003–4014 (2019).
23. Liu, Z. *et al.* Pdb-wide collection of binding data: current status of the pdbname database. *Bioinformatics* **31**, 405–412 (2015).
24. Smith, R. D. *et al.* Csar benchmark exercise of 2010: combined evaluation across all submitted scoring functions. *J. Chem. Inf. Model.* **51**, 2115–2131 (2011).
25. Ballester, P. J. & Mitchell, J. B. A machine learning approach to predicting protein–ligand binding affinity with applications to molecular docking. *Bioinformatics* **26**, 1169–1175 (2010).
26. Cao, D.-S., Xu, Q.-S. & Liang, Y.-Z. propy: a tool to generate various modes of chou’s pseaac. *Bioinformatics* **29**, 960–962 (2013).
27. Rogers, D. & Hahn, M. Extended-connectivity fingerprints. *J. Chem. Inf. Model.* **50**, 742–754 (2010).
28. Stepniewska-Dziubinska, M. M., Zielenkiewicz, P. & Siedlecki, P. Development and evaluation of a deep learning model for protein–ligand binding affinity prediction. *Bioinformatics* **34**, 3666–3674 (2018).
29. Zheng, L., Fan, J. & Mu, Y. Onionnet: a multiple-layer intermolecular-contact-based convolutional neural network for protein–ligand binding affinity prediction. *ACS Omega* **4**, 15956–15965 (2019).
30. Nguyen, T. *et al.* Graphdta: predicting drug–target binding affinity with graph neural networks. *Bioinformatics* **37**, 1140–1147 (2021).
31. Bai, P., Miljković, F., John, B. & Lu, H. Interpretable bilinear attention network with domain adaptation improves drug–target prediction. *Nat. Mach. Intell.* **5**, 126–136 (2023).
32. Danel, T. *et al.* Spatial graph convolutional networks. *Int. Conf. on Neural Inf. Process.* 668–675 (2020).
33. Wu, Z. *et al.* Representing long-range context for graph neural networks with global attention. *Int. Conf. on Neural Inf. Process. Syst.* **34**, 13266–13279 (2021).
34. Liu, M., Wang, Z. & Ji, S. Non-local graph neural networks. *IEEE Transactions on Pattern Analysis Mach. Intell.* **44**, 10270–10276 (2021).
35. Lim, J. *et al.* Predicting drug–target interaction using a novel graph neural network with 3d structure-embedded graph representation. *J. Chem. Inf. Model.* **59**, 3981–3988 (2019).
36. Yang, K. *et al.* Analyzing learned molecular representations for property prediction. *J. Chem. Inf. Model.* **59**, 3370–3388 (2019).
37. Maziarzka, Ł. *et al.* Molecule attention transformer. *arXiv preprint arXiv:2002.08264* (2020).
38. Gasteiger, J., Groß, J. & Günnemann, S. Directional message passing for molecular graphs. *Int. Conf. on Learn. Represent.* (2020).
39. Song, Y. *et al.* Communicative representation learning on attributed molecular graphs. *Int. Jt. Conf. on Artif. Intell.* 2831–2838 (2020).
40. Li, S. *et al.* Structure-aware interactive graph neural networks for the prediction of protein-ligand binding affinity. *ACM SIGKDD Conf. on Knowl. Discov. Data Min.* 975–985 (2021).
41. Li, S. *et al.* Giant: Protein-ligand binding affinity prediction via geometry-aware interactive graph neural network. *IEEE Transactions on Knowl. Data Eng.* **36**, 1991–2008 (2024).
42. Tsubaki, M., Tomii, K. & Sese, J. Compound–protein interaction prediction with end-to-end learning of neural networks for graphs and sequences. *Bioinformatics* **35**, 309–318 (2019).
43. Yang, S.-W. *et al.* Discovery of orally active pyrazoloquinolines as potent pde10 inhibitors for the management of schizophrenia. *Bioorganic & Medicinal Chem. Lett.* **22**, 235–239 (2012).
44. Dodson, C. A. *et al.* Crystal structure of an aurora-a mutant that mimics aurora-b bound to mln8054: insights into selectivity and drug design. *Biochem. J.* **427**, 19–28 (2010).
45. Norman, B. H. *et al.* Benzopyrans as selective estrogen receptor β agonists (serbas). part 4: Functionalization of the benzopyran a-ring. *Bioorganic & Medicinal Chem. Lett.* **17**, 5082–5085 (2007).

46. Berman, H. M. *et al.* The protein data bank. *Nucleic Acids Res.* **28**, 235–242 (2000).
47. Maveyraud, L. & Mourey, L. Protein x-ray crystallography and drug discovery. *Molecules* **25**, 1030 (2020).
48. Jumper, J. *et al.* Highly accurate protein structure prediction with alphafold. *Nature* **596**, 583–589 (2021).
49. Abramson, J. *et al.* Accurate structure prediction of biomolecular interactions with alphafold 3. *Nature* **630**, 493–500 (2024).
50. Zhong, Y. *et al.* Learning motif-based graphs for drug–drug interaction prediction via local–global self-attention. *Nat. Mach. Intell.* **6**, 1094–1105 (2024).
51. Gao, Z. *et al.* Hierarchical graph learning for protein–protein interaction. *Nat. Commun.* **14**, 1093 (2023).
52. Wang, Y. *et al.* Zerobind: a protein-specific zero-shot predictor with subgraph matching for drug-target interactions. *Nat. Commun.* **14**, 7861 (2023).
53. Li, M. *et al.* Dgl-lifesci: An open-source toolkit for deep learning on graphs in life science. *ACS Omega* **6**, 27233–27238 (2021).
54. Bordes, A., Usunier, N., Garcia-Durán, A., Weston, J. & Yakhnenko, O. Translating embeddings for modeling multi-relational data. *Int. Conf. on Neural Inf. Process. Syst.* 2787–2795 (2013).
55. Sun, Z., Deng, Z.-H., Nie, J.-Y. & Tang, J. Rotate: Knowledge graph embedding by relational rotation in complex space. *Int. Conf. on Learn. Represent.* .
56. Kingma, D. P. & Ba, J. Adam: A method for stochastic optimization. *Int. Conf. on Learn. Represent.* (2015).
57. Paszke, A. *et al.* Pytorch: An imperative style, high-performance deep learning library. *Int. Conf. on Neural Inf. Process. Syst.* (2019).
58. Wang, M. *et al.* Deep graph library: A graph-centric, highly-performant package for graph neural networks. *arXiv preprint arXiv:1909.01315* (2019).
59. Pedregosa, F. *et al.* Scikit-learn: Machine learning in python. *J. Mach. Learn. Res.* **12**, 2825–2830 (2011).
60. Harris, C. R. *et al.* Array programming with numpy. *Nature* **585**, 357–362 (2020).
61. Reback, J. *et al.* pandas-dev/pandas: Pandas 1.2. 4, zenodo (2021).
62. Landrum, G. Rdkit: Open-source cheminformatics. 2006. *Google Scholar* (2006).